JACS
JOURNAL OF THE AMERICAN CHEMICAL SOCIETY
pubs.acs.org/JACS
Article

Ester–Alkyl Linker-Regulated Molecular Folding in Head-to-Head Dimers Enabling >20% Efficiency in Organic Solar Cells

Xin Chen,[‖] Jie Wang,[‖] Jiong Yang, Tianchen Lu, Yupu Wang, Miaomiao Li,* Wendi Shi, Zhaoyang Yao, Xian-Kai Chen, Yanhou Geng, Xiangjian Wan,* and Yongsheng Chen*

Cite This: J. Am. Chem. Soc. 2026, 148, 10714–10724

Read Online

ACCESS | Metrics & More | Article Recommendations | Supporting Information

ABSTRACT: Dimeric acceptors have demonstrated significant potential for the simultaneous realization of high efficiency, good stability, and even stretchability in organic solar cells (OSCs). However, most dimeric acceptors suffer from compromised efficiency due to insufficient morphological control. Herein, we design and synthesize three head-to-head flexible alkyl-chain-linked dimeric acceptors, CH-E2, CH-E6, and CH-E10, along with their monomeric counterpart CH-E1, by systematically varying the alkyl linker lengths via esterification. This synthetic approach avoids conventional metal-catalyzed coupling reactions, eliminating the need for expensive catalysts and toxic intermediates, such as organotin reagents. Results demonstrate that the linker lengths critically govern molecular conformations, packing motifs, and aggregation behavior. The binary PM6:CH-E6 and ternary PM6:CH-E6:CH-E1 devices, benefiting from favorable film microstructures, enhanced charge carrier dynamics, and reduced E_{loss}, achieve PCEs of 19.17 and 20.14%, respectively. Furthermore, the flexible alkyl chain linkage inhibits molecular diffusion, thereby stabilizing the active layer morphology under thermal and mechanical stress. Thus, CH-E6-based devices exhibit significantly improved MPP operational stability and thermal endurance. The crack-onset strain (COS) of the PM6:CH-E6 blend film reaches 20%, twice that of PM6:CH-E1.

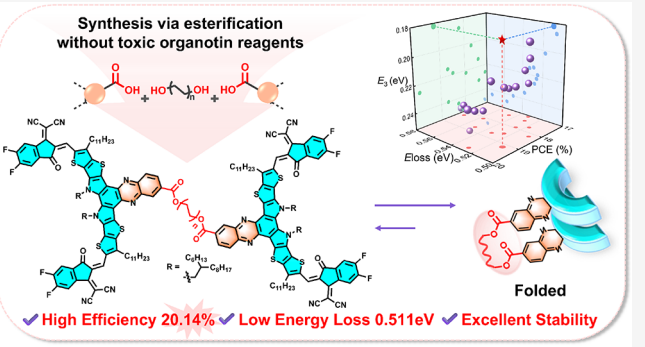

INTRODUCTION

Organic solar cells (OSCs) have emerged as a research hotspot in the field of renewable energy due to their flexibility, lightweight nature, and potential for large-scale, solution-processed manufacturing.[1−3] The development of small molecule acceptors (SMAs), particularly nonfullerene acceptors (NFAs), such as Y6 derivatives, has led to significant advancements in power conversion efficiency (PCE).[4−6] However, morphological degradation caused by the diffusion and aggregation of SMAs remains a major obstacle, severely compromising the stability of high-performance devices. Achieving both high efficiency and long-term stability thus remains a critical challenge for the commercialization of OSCs.[7−9] Dimer designs based on the Y6 framework have drawn increasing attention for their ability to suppress molecular diffusion and enhance the active layer morphological stability. Nonetheless, most existing dimers exhibit lower PCEs compared to their monomer counterparts, primarily due to unfavorable film morphology, which compromises charge transport and increases nonradiative recombination.[10] As such, the rational design of dimers that can simultaneously deliver high efficiency and enhanced stability represents a pressing research priority.

Researchers have ingeniously employed the limited linkage sites of monomers for dimerization, such as linking at end-groups, β-thiophene alkyl chains, or N-position alkyl chains.[11−15] Among them, head-to-head linkages at central core units are especially attractive, as they can preserve the $\pi-\pi$ stacking characteristics of terminal groups in monomeric units, offering potential advantages such as improved molecular packing and enhanced stability.[16] In recent years, researchers developed a series of high-performance CH-series acceptors featuring extended-conjugation quinoxaline central core units based on acceptor Y6, providing excellent design flexibility for constructing head-to-head linked dimers.[17] However, their synthesis primarily relies on conventional metal-catalyzed coupling reactions that require expensive catalysts and toxic intermediates, such as organotin reagents, which inherently limit structural diversity and compromise cost-effectiveness.[18−21]

Received: November 16, 2025
Revised: February 19, 2026
Accepted: February 24, 2026
Published: March 2, 2026

Downloaded via NANKAI UNIV on June 8, 2026 at 02:01:22 (UTC).
See https://pubs.acs.org/sharingguidelines for options on how to legitimately share published articles.

ACS Publications
© 2026 American Chemical Society

https://doi.org/10.1021/jacs.5c20384
J. Am. Chem. Soc. 2026, 148, 10714−10724

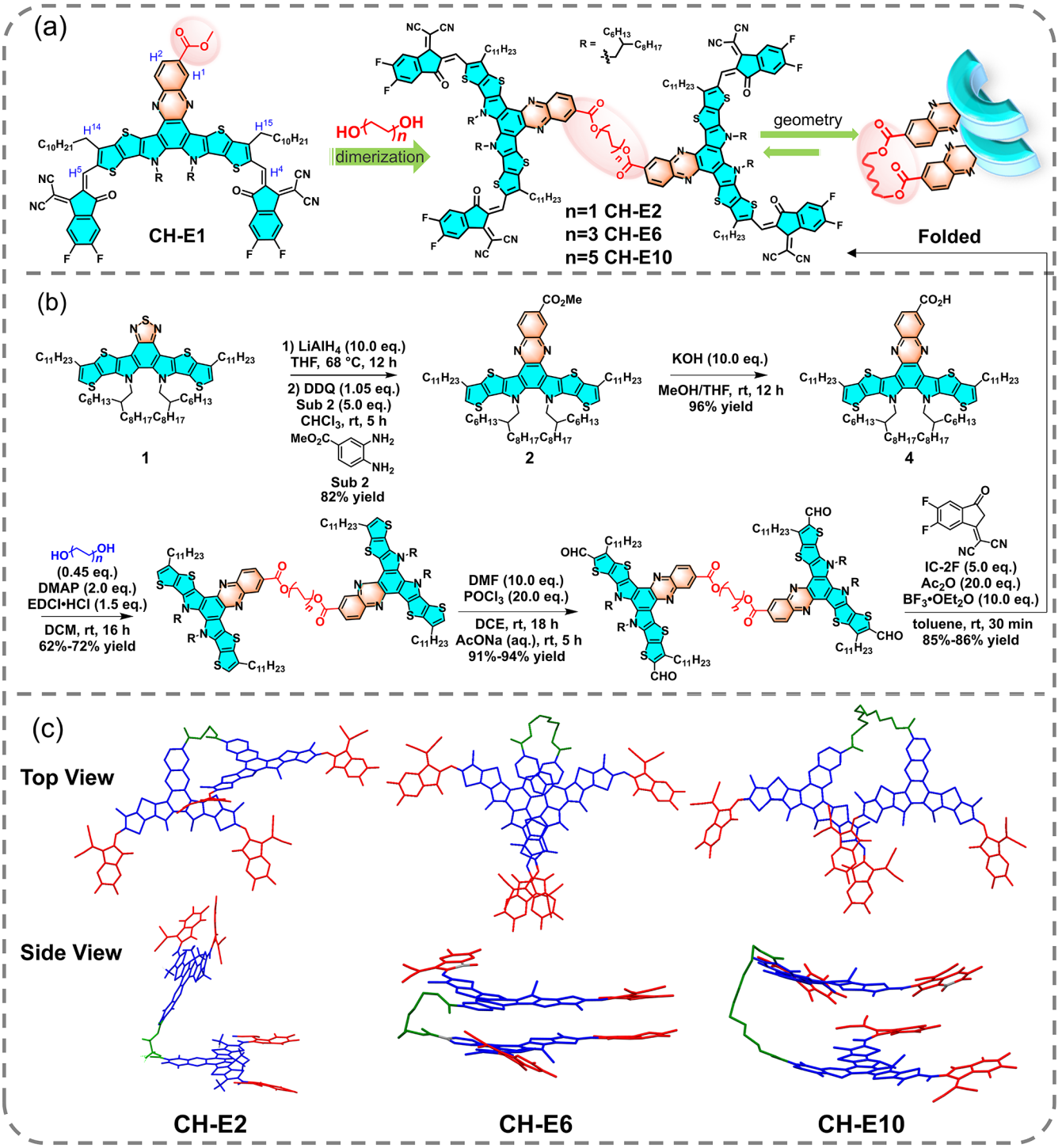

Figure 1. (a) Design strategy for the dimerized acceptors in this work. (b) Synthetic routes to the dimer acceptors CH-E2, CHE-6, and CH-10. (c) Snapshots of CH-E2, CH-E6, and CH-E10 structures extracted from MD simulations trajectories.

In this work, we present a simple and efficient strategy for dimer construction under mild conditions via esterification between the β-position methyl ester of the CH-phenazine central unit and diol compounds (Figure 1a). By tuning the alkyl chain lengths (C2, C6, C10), we synthesized a series of head-to-head flexible alkyl-chain-linked dimers: CH-E2, CH-E6, and CH-E10. The flexible alkyl linker serves as a pivotal "conformational modulator." By tuning the conformational freedom of the molecule, the linker length dictates the folded conformation of the three dimer acceptors. It has been found that the intramolecular preassembly conformation in solution governs molecular packing and blend morphology in the solid-state film, ultimately determining overall device performance. Among the three dimers, the C2 linker is too short, leading to significant steric hindrance that forces the molecule into a highly twisted conformation, and the C10 linker is too long, providing excessive conformational freedom. In contrast, CH-E6 with a C6 linker forms a compact folded conformation, enabling the formation of favorable film morphology with the highest crystallinity in the PM6:CH-E6 blend film. Con-

https://doi.org/10.1021/jacs.5c20384
J. Am. Chem. Soc. 2026, 148, 10714−10724

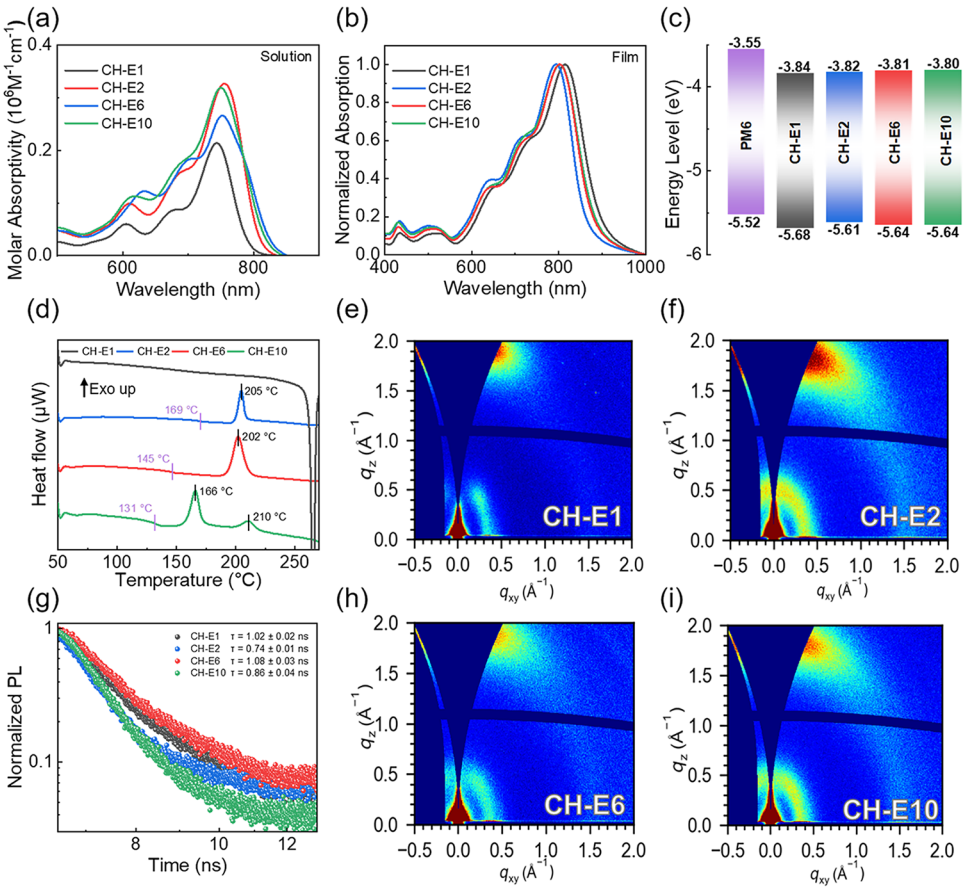

Figure 2. (a) UV−vis absorption spectra in chloroform solution. (b) Normalized UV−vis absorption spectra of the as-cast film. (c) Energy levels of active layer materials applied in this work. (d) Differential scanning calorimetry (DSC) thermograms of CH-E1 and the dimers with a heating rate of 10 °C min^{-1} under nitrogen atmosphere. (e) 2D grazing-incidence wide-angle X-ray scattering (GIWAXS) images of the as-cast films of CH-E1. (f) The 2D GIWAXS images of the as-cast films of CH-E2. (g) Time-resolved photoluminescence (PL) decay traces of neat films measured under 760 nm excitation. The average values and standard deviations were calculated from at least 4 independent devices. (h) The 2D GIWAXS images of the as-cast films of CH-E6. (i) The 2D GIWAXS images of the as-cast films of CH-E10.

sequently, the binary PM6:CH-E6 device exhibits a PCE of 19.17%, surpassing that of the monomer CH-E1 (18.81%), representing a rare case in which a dimer outperforms its monomer counterpart. Further incorporating CH-E1 into the PM6:CH-E6 system improved the PCE to 20.14%. Particularly, both binary and ternary OSCs based on the dimeric acceptor exhibit suppressed nonradiative recombination (ΔE_3 = 0.182 eV) compared to the monomer counterparts, leading to a significantly reduced energy loss (E_{loss} = 0.511 eV). More importantly, chain entanglement effects induced by the dimer structure synergistically boost the operational stability and mechanical durability.

RESULTS AND DISCUSSION

Material Synthesis and Characterization

The three dimeric acceptors, CH-E2, CH-E6, and CH-E10 with varying flexible linker lengths, were synthesized as illustrated in Figure 1a,b and the Supporting Information. Starting from the commercially available precursor 1, intermediate compound 2 was obtained in satisfactory yield following procedures reported in our previous work.[22,23] Subsequent hydrolysis of compound 2 under alkaline conditions afforded compound 4. Notably, the key dimeric scaffold was synthesized via esterification of compound 4 with various diol compounds. The introduction of flexible alkyl linkers not only enables the formation of dimeric structures but also ensures good solubility in common solvents such as chloroform and toluene (Figure S1 and Table S1). Thermogravimetric analysis (TGA) revealed decomposition temperatures (T_d, 5% weight loss) over 320 °C for all four molecules, indicating their good thermal stability (Figure S2 and Table S2).

To systematically investigate the effect of alkyl linker length on molecular conformation, we performed classical molecular dynamics (MD) simulations combined with density functional theory (DFT) calculations on the dimers. The calculation results (Figure 1c) show that the three dimers exhibit distinct conformations. CH-E2 exhibits a highly twisted conformation. Conversely, the subunits of CH-E6 and CH-E10 tend to adopt similar face-to-face folded conformations with small dihedral angles. The calculated binding energies between the two covalently linked monomeric units for CH-E6 (−29.41 kJ mol^{-1}) and CH-E10 (−16.55 kJ mol^{-1}) are significantly more negative than those of CH-E2 (−1.45 kJ mol^{-1}). A more negative binding energy implies a deeper potential that is harder to disrupt.[24] The results indicate that both CH-E6 and CH-E10, particularly the former, are thermodynamically favored to form and maintain stable folded conformations.

To characterize the three-dimensional (3D) structures of the dimers, we performed two-dimensional proton−proton nuclear

https://doi.org/10.1021/jacs.5c20384
J. Am. Chem. Soc. 2026, 148, 10714−10724

Overhauser effect spectroscopy (2D ^{1}H−^{1}H NOESY NMR) measurements. As depicted in Figures S3−S6, CH-E1 only exhibited interactions between the vinylic protons (labeled H^4/H^5) and the β-protons (labeled H^{14}/H^{15}) of the thiophene rings, owing to their close spatial proximity. Similar to CH-E1, CH-E2 showed exclusively the aforementioned proton correlations with no additional signals detected, indicating the absence of an intramolecular folded conformation. In contrast, CH-E6 and CH-E10 displayed distinct NOE correlations between protons H^4/H^5 and multiple alkyl chain protons, confirming the occurrence of intramolecular conformational folding. Notably, CH-E6 exhibited more pronounced behavior: its central unit protons (labeled H^1 and H^2) each showed NOE interactions with protons of several alkyl chains, suggesting a higher degree of overlap between molecular fragments.

Furthermore, the results of temperature-dependent ^{1}H NMR (Figures S7−S10) revealed that, upon increasing the temperature, the peaks of CH-E2, CH-E6, and CH-E10 became progressively sharper and more symmetric compared with those of CH-E1. Among these derivatives, CH-E6 showed the most significant changes. Its central unit proton H^1 underwent a pronounced downfield shift with increasing temperature. This observation indicates that H^1 was subject to shielding effects from another intramolecular fragment at low temperatures, whereas the molecular conformation unfolded upon heating, leading to a substantial enhancement of the deshielding effect. These findings are consistent with the DFT calculation results presented above.[25,26]

In dilute solution, the UV−vis absorption spectra of the dimers (Figures 2a and S11 and Table S3) exhibited red shifts, relative to that of the monomeric acceptor CH-E1, with maximum absorption peaks (λ_{max}) observed at 744, 755, 753, and 750 nm for CH-E1, CH-E2, CH-E6, and CH-E10, respectively. The molar extinction coefficients (ε) for CH-E1, CH-E2, CH-E6, and CH-E10 are 2.08×10^5, 3.31×10^5, 2.82×10^5, and 3.08×10^5 M^{-1} cm^{-1}, which are consistent with calculated oscillator strengths with values of 1.242, 1.923, 1.466, and 2.120, respectively. In addition, the dimers showed more pronounced vibrational fine structure in the 600−700 nm range compared to CH-E1. The red-shifted absorption and observed vibronic peaks suggest the existence of intramolecular aggregation in the dimers.[27,28] Furthermore, fitting the vibronic progression (Figure S12) reveals that CH-E6 and CH-E10, particularly the former, exhibit a shoulder peak absorption at approximately 790 nm, a feature not observed for CH-E1 and CH-E2. This further corroborates the strong electronic coupling effect induced by the folded conformation.[29]

The temperature-dependent UV−vis measurement results indicate that all dimer maximum absorption peaks exhibit a blue shift, toward the absorption of the monomeric CH-E1 (Figure S13). In contrast, there is nearly no change in the CH-E1 maximum absorption peak with increasing temperature, indicating negligible aggregation.[30] Moreover, as the temperature increased from 20 to 55 °C, the shoulder peaks of CH-E6 and CH-E10 disappeared. These results indicate that an intramolecular folding or unfolding conformation is responsible for the observed absorption spectral features.

Moreover, we conducted TD-DFT calculations to clarify the photophysical origin of the additional vibronic feature in CH-E6 and CH-E10. The calculated S_1 transition for CH-E2 is approximately 740 nm, whereas that for CH-E6 and CH-E10 is approximately 790 nm. These theoretical results are in good agreement with the peak positions and intensity trends obtained from multiple Gaussian fittings of the experimental solution absorption spectra. Consequently, the natural transition orbital (NTO) analysis indicates that the additional vibronic feature arises from intramolecular through space charge transfer between the two subunits (Figure S14 and Table S4).

In the solid films, the dimers exhibited 12−21 nm blue shifts in the maximum absorption peak relative to CH-E1 (Figure 2b), indicating suppressed molecular packing during film formation due to increased segment size. Compared to CH-E2 film, CH-E6 and CH-E10 films showed progressively red-shifted maximum absorptions, reflecting increased aggregation and intermolecular interactions likely attributable to their face-to-face folded conformation. Cyclic voltammetry measurements revealed that the three dimers possessed similar lowest unoccupied molecular orbital (LUMO) energy levels, with slight upshifts compared to CH-E1 (Figure 2c), which may contribute to higher open-circuit voltages (V_{OC}) in photovoltaic devices.

Differential scanning calorimetry (DSC) measurements were performed to investigate the crystallinity differences for the four acceptors (Figure 2d). The cold crystallization temperature (T_{cc}) marks the transition of a material from an amorphous to a crystalline state before melting during the heating process.[31,32] As the linker length increases, the dimers exhibit a progressive decrease in T_{cc} and broadening of the cold crystallization peak. Specifically, CH-E2 and CH-E6 displayed T_{cc} values of 205 and 202 °C, respectively, while CH-E10 showed dual cold crystallization peaks at 166 and 210 °C. The presence of two distinct crystallization peaks for CH-E10 likely arises from the increased conformational freedom provided by its longer alkyl linker, which facilitates stepwise crystallization behavior.[33] In contrast to the dimers, the monomer CH-E1 exhibits a clear melting point (T_m) at 265 °C with a melting enthalpy (ΔH_m) of 22.5 J/g, whereas the T_m values of the dimers were not detected, as they exceeded the test range of 50−270 °C.

To investigate the molecular stacking and crystallinity of the neat films, grazing-incidence wide-angle X-ray scattering (GIWAXS) measurements were conducted. The 2D GIWAXS patterns, along with the corresponding in-plane (IP) and out-of-plane (OOP) line-cut profiles, are shown in Figures 2e,f,h,i and S15, while the extracted crystallographic parameters are summarized in Table S5. All films displayed distinct (010) diffraction peaks in the OOP direction and (100) peaks in the IP direction, indicating a predominant face-on molecular orientation favorable for vertical charge transport in OSCs. Compared to the monomer ($d_{\pi-\pi}$ = 3.46 Å, CCL = 17.67 Å), CH-E2 ($d_{\pi-\pi}$ = 3.66 Å, CCL = 16.53 Å) exhibits weakened $\pi-\pi$ stacking and crystallinity due to steric hindrance from its larger dihedral angle between the two subunits. In contrast, CH-E6 ($d_{\pi-\pi}$ = 3.40 Å, CCL = 18.42 Å) and CH-E10 ($d_{\pi-\pi}$ = 3.50 Å, CCL = 17.73 Å) demonstrate interlayer lattice ordering matching or surpassing that of the monomer, which is attributed to face-to-face conformations (as discussed in the above DFT calculations). This enhanced ordering is expected to favor efficient electron transport. The compact and ordered molecular packings are known to facilitate extended exciton lifetimes (τ).[34,35] Thus, it is reasonable to observe that CH-E6 exhibits a slightly larger τ of 1.08 ± 0.03 ns compared to that of CH-E2 (0.74 ± 0.01 ns), CH-E10 (0.86 ± 0.04 ns), and CH-E1 (1.02 ± 0.02 ns) (Figure 2g). The improved molecular

https://doi.org/10.1021/jacs.5c20384
J. Am. Chem. Soc. 2026, 148, 10714−10724

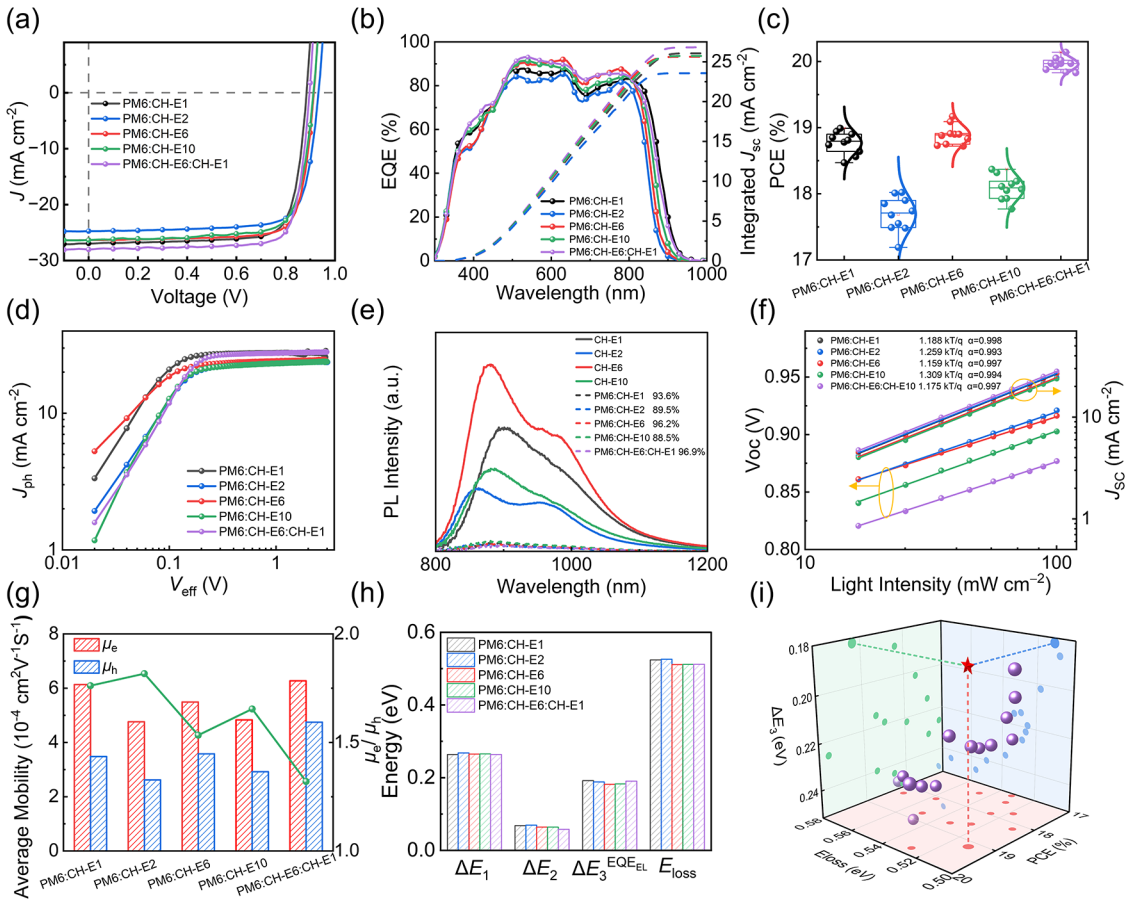

Figure 3. (a) $J-V$ characteristics and (b) EQE curves of devices based on PM6:CH-E1, PM6:dimer, and PM6:CH-E6:CH-E1, (c) device efficiency normal distribution chart of corresponding devices, (d) $J_{ph}-V_{eff}$ curves of devices based on PM6:CH-E1, PM6:dimer, and PM6:CH-E6:CH-E1, (e) PL spectra of neat and blend films indicating efficiencies of PL quenching, (f) J_{SC} versus light intensity and V_{OC} versus light intensity, (g) hole and electron mobilities, (h) E_{loss} and three detailed parts of ΔE_1, ΔE_2, and ΔE_3 values of devices based on PM6:CH-E1, PM6:dimers, and PM6:CH-E6:CH-E1, and (i) photovoltaic performance parameters of OSCs based on flexible linked dimers.

Table 1. Summary of the Optimal Photovoltaic Parameters of OSCs with a Conventional Device Structure[a]

active layer	V_{OC} (V)	J_{SC} (mA cm^{-2})	J_{SC}[b] (mA cm^{-2})	FF (%)	PCE (%)
PM6:CH-E1	0.885	26.95	26.07	78.81	18.81
	0.885 ± 0.002	26.66 ± 0.21		79.30 ± 0.48	18.73 ± 0.11
PM6:CH-E2	0.933	24.73	23.57	77.83	18.01
	0.931 ± 0.002	24.45 ± 0.26		77.88 ± 0.32	17.78 ± 0.20
PM6:CH-E6	0.914	26.32	25.64	79.48	19.17
	0.912 ± 0.003	26.33 ± 0.29		78.57 ± 0.69	18.88 ± 0.15
PM6:CH-E10	0.913	26.35	25.74	76.39	18.37
	0.915 ± 0.003	25.92 ± 0.32		76.22 ± 0.67	18.09 ± 0.18
PM6:CH-E6:CH-E1	0.897	28.03	26.82	80.12	20.14
	0.893 ± 0.003	27.94 ± 0.31		80.00 ± 0.38	19.96 ± 0.09

[a]The average values and standard deviations were calculated from at least 10 independent devices. [b]Integrated J_{SC} from EQE curve.

stacking order in its film is also conducive to suppressing nonradiative recombination in the resulting OSCs, which will be discussed in detail in the subsequent section.

Photovoltaic Performance

Conventional structure devices with a configuration of ITO/2PACz/PM6:acceptor/PNDIT-F3N/Ag were fabricated to investigate the photovoltaic performances of these acceptors. The optimized current density−voltage ($J-V$) curves are presented in Figure 3a, and the relevant photovoltaic parameters are summarized in Table 1. The optimal device based on CH-E6 demonstrated a PCE of 19.17% with a V_{OC} of 0.914 V, a J_{SC} of 26.32 mA cm^{-2}, and an FF of 79.48%. In contrast, the control device based on monomeric CH-E1 exhibited a PCE of 18.81%, with a V_{OC} of 0.885 V, a J_{SC} of 26.95 mA cm^{-2}, and an FF of 78.81%. Compared with the monomer CH-E1-based device, dimer-based devices achieved higher V_{OC} values, with the CH-E2-based device exhibiting the highest V_{OC} of 0.933 V, though its PCE slightly decreased to 18.01% due to a relatively lower J_{SC} of 24.73 mA cm^{-2} and a lower FF of 77.83%. The CH-E10-based device exhibited a PCE of 18.37% with a V_{OC} of 0.913 V, a J_{SC} of 26.35 mA cm^{-2}, and an FF of 76.39%. Clearly, the alkyl linker length of these

https://doi.org/10.1021/jacs.5c20384
J. Am. Chem. Soc. 2026, 148, 10714−10724

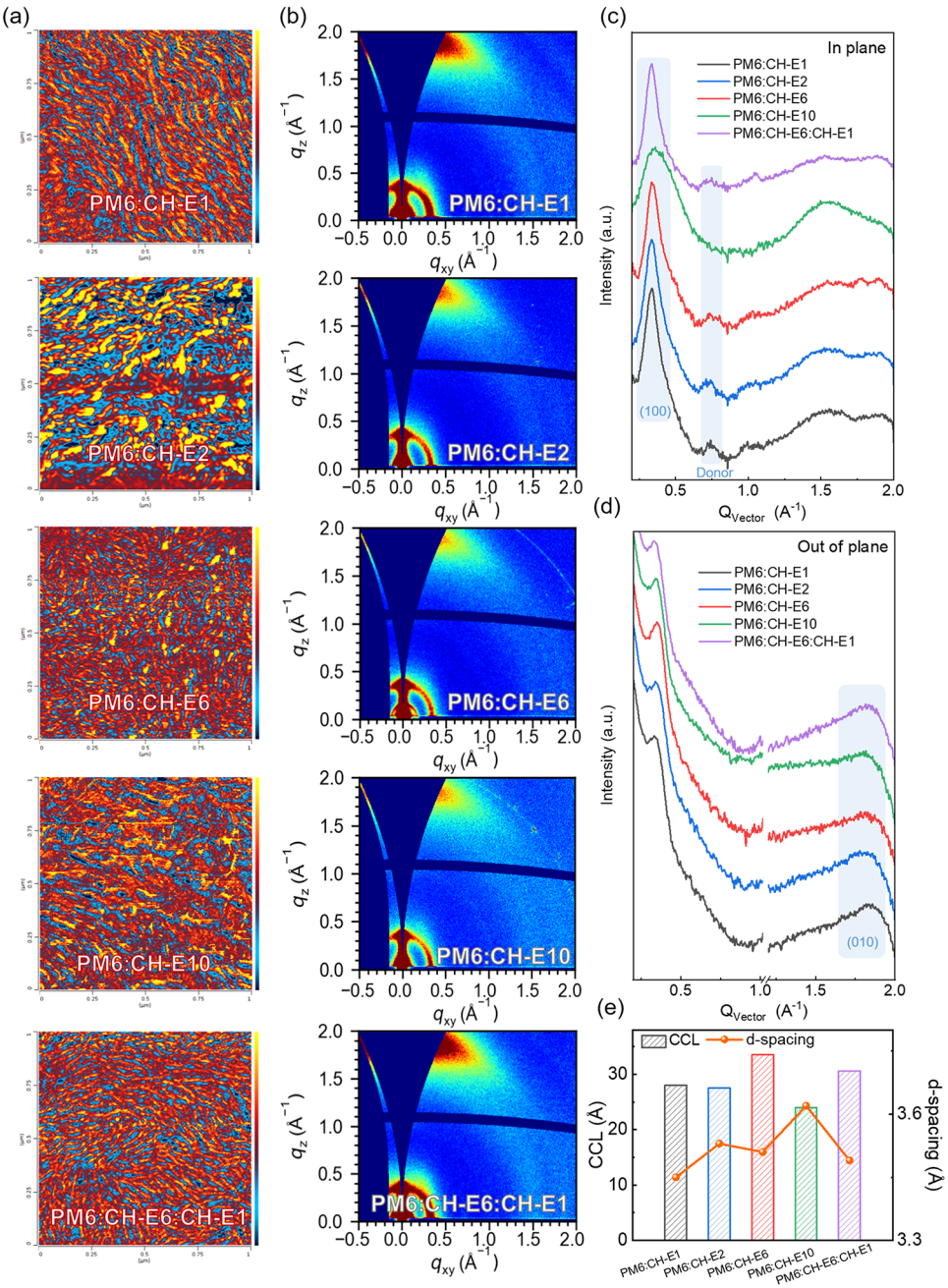

Figure 4. (a) AFM-IR images of the blend films. The donor and acceptor domains were marked with blue and red colors, respectively. Note that the different appearance of PM6:CH-E2 arises from its high signal intensity in the image plot using "cold-to-warm" color scale, which has no effect on the result analysis. (b) 2D GIWAXS images of the blend films. (c) IP and OOP line-cut curves of the blend films. (d) Histogram of the *d*-spacing and CCLs of the blend films variation derived from GIWAXS measurements in out-of-plane direction. (e) Statistical fibril diameters in blend films.

dimers significantly influences their photovoltaic performance. Compared to the other two dimer acceptors, CH-E6 showed the improved FF and the best PCE, which could be correlated with its enhanced charge generation and transport dynamics, as discussed below. The incorporation of a third component serves as an effective strategy to synergistically enhance device efficiency and stability. By introducing the dimer CH-E6 alongside the monomer CH-E1, the ternary device achieved a remarkable PCE of 20.14% with a V_{OC} of 0.897 V, a J_{SC} of 28.03 mA cm^{-2}, and an FF of 80.12%. Figure 3b illustrates the external quantum efficiency (EQE) curves for the binary and ternary devices, showing a progressive red shift in the absorption edges from the PM6:CH-E2 to PM6:CH-E10 devices, correlating well with the variations observed in the UV−vis absorption spectra. In comparison to the binary devices, the ternary device demonstrated significantly enhanced EQE, supporting the increase of J_{SC}. Figure 3c shows the statistical distributions of the PCE, demonstrating good reproducibility of the results.

The properties of charge generation, transport, and recombination in the five devices were investigated through a series of tests. First, to investigate the charge generation and dissociation processes, the photocurrent density (J_{ph}) versus the effective voltage (V_{eff}) was examined. The charge

https://doi.org/10.1021/jacs.5c20384
J. Am. Chem. Soc. 2026, 148, 10714−10724

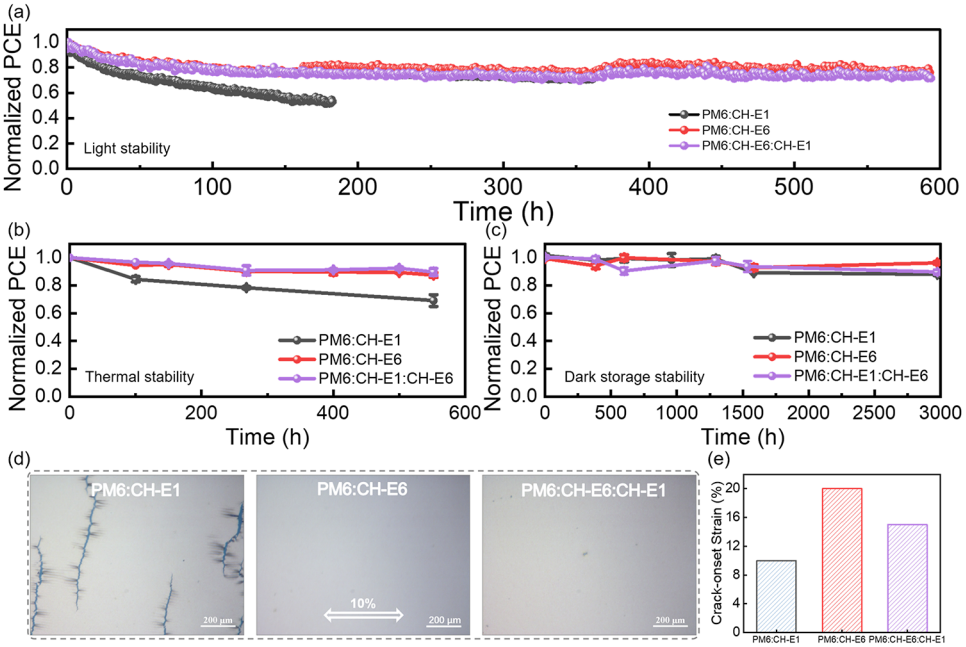

Figure 5. Stability measurement of unencapsulated devices in a N_2 atmosphere. (a) MPP stability under 1 sun illumination, (b) thermal stability at 65 °C, and (c) dark storage stability. (d) Optical micrographs of the formed cracks of three blend films by stretching on poly(dimethylsiloxane) (PDMS) substrates at 10% strains. (e) Crack-onset strain values of corresponding blend films.

dissociation efficiency (η_{diss}) is estimated as the ratio of J_{ph} under short-circuit conditions to the saturation photocurrent density (J_{sat}), and charge collection efficiency (η_{coll}) is calculated as the ratio of J_{ph} under maximum power output conditions to J_{sat}. As shown in Figure 3d, the performance of the CH-E6-based binary device (η_{diss} = 97.18% and η_{coll} = 88.53%) is superior to that of the CH-E2-based binary device (η_{diss} = 97.44% and η_{coll} = 86.46%) and the CH-E10-based binary device (η_{diss} = 96.94% and η_{coll} = 87.30%). The ternary device exhibited the best η_{diss} (97.98%) and η_{coll} (90.15%) values. The higher values of η_{diss} and η_{coll} indicate improved efficiencies in the processes of exciton dissociation and charge collection, which contribute to the increased J_{SC} and FF observed in both CH-E6-based binary and ternary devices.[36] Meanwhile, photoluminescence (PL) spectroscopy measurements were conducted to further investigate the exciton dissociation processes (Figures 3e and S16).[37] The PM6:CH-E6 blend exhibited a significantly higher PL quenching efficiency (97.6/96.2%), compared to PM6:CH-E2 (94.0/89.5%) and PM6:CH-E10 (94.4/88.5%), excited at 550/760 nm.

Furthermore, bimolecular recombination was revealed by measuring $J-V$ curves under different light intensity (P_{light}).[38] Exponential factor (α) of the power-law equation $J_{SC} \propto P_{light}^{\alpha}$ can be used to analyze the bimolecular recombination in OSCs. As shown in Figure 3f, the obtained α values approaching 1 for all devices demonstrate suppressed bimolecular recombination. Additionally, the $V_{oc} \propto (nkT/q)\ln(P_{light})$ relation, where S is defined as nkT/q, can estimate the trap-assisted recombination loss in the OSCs. The CH-E6-based binary and ternary devices exhibited S values of 1.159 and 1.175 kT/q, respectively, which were lower than those of the CH-E2-based devices (1.259 kT/q) and CH-E10-based devices (1.309 kT/q).

The hole (μ_h) and electron mobilities (μ_e) were characterized through space-charge-limited current (SCLC) measurements (Figures 3g and S17 and Table S6). The calculated values of μ_h/μ_e are $6.13 \times 10^{-4}/3.48 \times 10^{-4}$ cm^2 V^{-1} s^{-1} for PM6:CH-E1, $4.76 \times 10^{-4}/2.62 \times 10^{-4}$ cm^2 V^{-1} s^{-1} for PM6:CH-E2, $5.49 \times 10^{-4}/3.58 \times 10^{-4}$ cm^2 V^{-1} s^{-1} for PM6:CH-E6, and $4.83 \times 10^{-4}/2.92 \times 10^{-4}$ cm^2 V^{-1} s^{-1} for PM6:CH-E10, demonstrating that dimers with an optimized flexible linker length enhance charge transport. The PM6:CH-E6:CH-E1 ternary blend achieved the highest μ_h/μ_e values ($6.27 \times 10^{-4}/4.75 \times 10^{-4}$ cm^2 V^{-1} s^{-1}) and a more balanced μ_h and μ_e with a μ_h/μ_e ratio of 1.32. These results reveal that the ternary device has more efficient exciton dissociation and charge transport, as well as suppressed charge recombination in comparison to the binary devices, collectively enhancing both J_{SC} and FF.

Meanwhile, energy loss (E_{loss}) of the devices was evaluated according to the Shockley–Queisser (SQ) theory.[39−41] The detailed results are presented in Table S7. For PM6:CH-E1, PM6:CH-E2, PM6:CH-E6, PM6:CH-E10, and PM6:CH-E6:CH-E1 systems, the E_g values were determined through derivative analysis of the highly sensitive EQE spectra, yielding values of 1.409, 1.459, 1.425, 1.425, and 1.409 eV, respectively. These correspond to overall E_{loss} values of 0.524, 0.526, 0.511, 0.512, and 0.512 eV, respectively. A comparative analysis of the E_{loss} parameters is provided in Figure 3h. Especially, the ΔE_3 values (i.e., nonradiative energy loss), calculated using the equation $\Delta E_3 = -kT\ln(EQE_{EL})$, were determined to be 0.192, 0.188, 0.182, 0.183, and 0.190 eV for PM6:CH-E1, PM6:CH-E2, PM6:E6, PM6:E10, and PM6:CH-E6:CH-E1 devices (Figure S18), respectively. To the best of our knowledge, the ΔE_3 of 0.182 eV is one of the lowest nonradiative recombination loss values reported for flexible linked dimeric acceptors to date (Figure 3i and Table S8).

Morphology Analysis

To explore the relationship between the active layer morphology and device performance, atomic force microscopy-based infrared spectroscopy (AFM-IR) was employed to

https://doi.org/10.1021/jacs.5c20384
J. Am. Chem. Soc. 2026, 148, 10714−10724

investigate the nanoscale morphology of the blend films. As shown in Figure 4a, AFM-IR signals of the blend films were recorded by probing the characteristic C≡N stretching vibration (2216 cm^{-1}) originating from acceptors, and the D/A interpenetrating fibrillary networks are clearly observable. PM6:CH-E2 exhibits a smaller phase separation than PM6:CH-E1 due to weaker self-aggregation of CH-E2, arising from steric hindrance caused by its molecular conformation. In contrast, PM6:CH-E10 showed excessive phase separation. The CH-E6-based binary and ternary blends demonstrated optimized phase separation scales, resulting in superior charge transport properties.[42] Furthermore, a statistical analysis of the nanofiber sizes was conducted. As shown in Figure S19, PM6:CH-E6:CH-E1 exhibits an optimal fiber size of ≈16.2 nm, compared with ≈14.2, ≈11.4, ≈15.3, and ≈17.3 nm for PM6:CH-E1, PM6:CH-E2, PM6:CH-E6, and PM6:CH-E10, respectively. 2D GIWAXS was used to investigate the crystallinity properties of the blend films. As shown in Figure 4b, the five blend films exhibited clear (010) diffraction peaks in the OOP direction, indicating a face-on orientation preference. The peak at 0.7 $Å^{-1}$ observed in the IP cut-lines is attributed to the (100) diffraction of PM6 (Figure S15). The line-cut curve analysis further revealed that the molecular packing and crystallization tendency of the blend films resemble those of the neat acceptor (Figure 4c−e and Table S5). Among them, the PM6:CH-E6 ($d_{\pi-\pi}$ = 3.34 Å, CCL = 29.33 Å) and PM6:CH-E6:CH-E1 ($d_{\pi-\pi}$ = 3.36 Å, CCL = 30.40 Å) systems demonstrate higher molecular packing density and extended structural order in the OOP direction, which is consistent with their high charge carrier mobility and AFM-IR measurement data.

Stability and Mechanical Properties of OSCs

Given the high efficiency of the CH-E6-based binary and ternary devices, we conducted a systematic comparison of their operational stability relative to that of the monomer-based CH-E1 device. Maximum power point (MPP) tracking was performed on unencapsulated devices under one-sun white LED illumination in a nitrogen-filled glovebox, with normalized PCEs presented in Figure 5a. The CH-E1-based device exhibited a rapid performance decline, with the PCE dropping by over 40% after 90 h of continuous operation, indicative of typical light-induced burn-in degradation. In contrast, CH-E6-based binary and ternary devices showed significantly suppressed burn-in losses during the same period. After an initial stabilization phase within the first 90 h, the CH-E6 binary and ternary devices retained 80% of their initial PCE, and maintained this stability over a subsequent extended testing period of 500 h with less than 10% further degradation in PCE. Further stability evaluation under thermal stress in the dark reinforced this trend (Figure 5b). Both binary and ternary CH-E6-based devices maintained over 90% of their initial PCE after 550 h of aging (linearly extrapolate T_{80} beyond 1380 h, Figure S20), while CH-E1-based devices suffered a PCE loss of approximately 40%. Additionally, negligible differences in performance under dark storage conditions (Figure 5c) indicate that the observed degradation predominantly results from morphological evolution during device operation.

Furthermore, the CH-E6 molecule incorporates a flexible alkyl linker that likely anchors adjacent molecules, forming an entangled network that restricts excessive molecular migration under thermal stress and, thereby, stabilizes the phase-separated morphology. To validate this hypothesis, a pseudo-free-standing tensile test was performed, and the extracted crack-onset strain (COS) values are presented in Figure 5e.[43,44] As shown in Figure 5d, at a 10% strain threshold, PM6:CH-E1 films exhibited pronounced cracking, whereas PM6:CH-E6 films remained intact and smooth. Remarkably, the ternary blend PM6:CH-E6:CH-E1 also maintained structural integrity under the same strain. The results indicate that the entanglement effect induced by CH-E6 within PM6:CH-E1 enhances both the morphological stability and the mechanical ductility of the active layer.

CONCLUSIONS

In summary, this work reported the design and synthesis of three dimeric acceptors, CH-E2, CH-E6, and CH-E10 with systematically varied flexible linker lengths via efficient esterification, along with their monomeric counterpart CH-E1. This synthetic route avoids expensive catalysts and toxic intermediates, such as organotin reagents. By optimization of the length of the connecting chain, the molecular conformation can be regulated. The short-chain CH-E2 exhibited a torsional conformation that weakened the intramolecular interactions and impaired intermolecular packing, while the long-chain CH-E10 experienced excessive crystallization due to increased conformational flexibility. In contrast, the C6 linker strikes a balance between conformational freedom and locking, leading to a compact folded conformation in CH-E6, allowing for the formation of optimally sized crystalline domains when blended with PM6. This yields a well-defined nanofibrillar interpenetrating network. Such optimized morphology maximizes exciton dissociation efficiency, enhances charge collection, and suppresses nonradiative recombination, ultimately yielding high device performance. As a result, the binary device based on PM6:CH-E6 achieved a PCE of 19.17%, higher than that of its monomer-based counterpart, the CH-E1-based device. Furthermore, the ternary blend system PM6:CH-E6:CH-E1 further improved the device PCE to 20.14% along with enhanced MPP operational stability and thermal endurance. Additionally, the incorporation of a flexible linker in CH-E6 facilitates molecular entanglement, leading to an enhanced mechanical robustness of the blend film. Overall, this study highlights the effectiveness of adjusting flexible linker lengths within the central core units as a strategy to simultaneously improve efficiency, stability, and mechanical property in OSCs.

ASSOCIATED CONTENT

Supporting Information

The Supporting Information is available free of charge at https://pubs.acs.org/doi/10.1021/jacs.5c20384.

Materials and characterization methods, material synthesis, device fabrication and measurement, NMR and HR-MS spectra, UV−vis absorption spectra, DFT calculations, charge mobility, additional tables, etc. (PDF)

AUTHOR INFORMATION

Corresponding Authors

Miaomiao Li − *School of Materials Science and Engineering, State Key Laboratory of Advanced Materials for Intelligent Sensing, Tianjin Key Laboratory of Molecular Optoelectronic Science and Key Laboratory of Organic Integrated Circuits, Ministry of Education, Tianjin University, Collaborative*

https://doi.org/10.1021/jacs.5c20384
J. Am. Chem. Soc. 2026, 148, 10714−10724

Innovation Center of Chemical Science and Engineering (Tianjin), Tianjin 300072, China; orcid.org/0000-0003-2481-0326; Email: miaomiao.li@tju.edu.cn

Xiangjian Wan − *State Key Laboratory of Elemento-Organic Chemistry, Key Laboratory of Functional Polymer Materials, College of Chemistry, Renewable Energy Conversion and Storage Center (RECAST), Nankai University, Tianjin 300071, China;* orcid.org/0000-0001-5266-8510; Email: xjwan@nankai.edu.cn

Yongsheng Chen − *State Key Laboratory of Elemento-Organic Chemistry, Key Laboratory of Functional Polymer Materials, College of Chemistry, Renewable Energy Conversion and Storage Center (RECAST), Nankai University, Tianjin 300071, China;* orcid.org/0000-0003-1448-8177; Email: yschen99@nankai.edu.cn

Authors

Xin Chen − *State Key Laboratory of Elemento-Organic Chemistry, Key Laboratory of Functional Polymer Materials, College of Chemistry, Renewable Energy Conversion and Storage Center (RECAST), Nankai University, Tianjin 300071, China*

Jie Wang − *State Key Laboratory of Elemento-Organic Chemistry, Key Laboratory of Functional Polymer Materials, College of Chemistry, Renewable Energy Conversion and Storage Center (RECAST), Nankai University, Tianjin 300071, China*

Jiong Yang − *State Key Laboratory of Elemento-Organic Chemistry, Key Laboratory of Functional Polymer Materials, College of Chemistry, Renewable Energy Conversion and Storage Center (RECAST), Nankai University, Tianjin 300071, China*

Tianchen Lu − *Institute of Functional Nano & Soft Materials (FUNSOM), Joint International Research Laboratory of Carbon-Based Functional Materials and Devices, State Key Laboratory of Bioinspired interfacial Materials Science, Soochow University, Suzhou, Jiangsu 215123, China*

Yupu Wang − *School of Materials Science and Engineering, State Key Laboratory of Advanced Materials for Intelligent Sensing, Tianjin Key Laboratory of Molecular Optoelectronic Science and Key Laboratory of Organic Integrated Circuits, Ministry of Education, Tianjin University, Collaborative Innovation Center of Chemical Science and Engineering (Tianjin), Tianjin 300072, China*

Wendi Shi − *State Key Laboratory of Elemento-Organic Chemistry, Key Laboratory of Functional Polymer Materials, College of Chemistry, Renewable Energy Conversion and Storage Center (RECAST), Nankai University, Tianjin 300071, China*

Zhaoyang Yao − *State Key Laboratory of Elemento-Organic Chemistry, Key Laboratory of Functional Polymer Materials, College of Chemistry, Renewable Energy Conversion and Storage Center (RECAST), Nankai University, Tianjin 300071, China;* orcid.org/0000-0003-1384-183X

Xian-Kai Chen − *Institute of Functional Nano & Soft Materials (FUNSOM), Joint International Research Laboratory of Carbon-Based Functional Materials and Devices, State Key Laboratory of Bioinspired interfacial Materials Science, Soochow University, Suzhou, Jiangsu 215123, China;* orcid.org/0000-0002-8580-7246

Yanhou Geng − *School of Materials Science and Engineering, State Key Laboratory of Advanced Materials for Intelligent Sensing, Tianjin Key Laboratory of Molecular Optoelectronic Science and Key Laboratory of Organic Integrated Circuits, Ministry of Education, Tianjin University, Collaborative Innovation Center of Chemical Science and Engineering (Tianjin), Tianjin 300072, China;* orcid.org/0000-0002-4997-3925

Complete contact information is available at: https://pubs.acs.org/10.1021/jacs.5c20384

Author Contributions

[‖]X.C. and J.W. contributed equally to this work.

Notes

The authors declare no competing financial interest.

■ ACKNOWLEDGMENTS

The authors gratefully acknowledge the financial support from the Fundamental and Interdisciplinary Disciplines Breakthrough Plan of the Ministry of Education of China (JYB2025XDXM410), the Ministry of Science and Technology of China (2022YFB4200400), and the National Natural Science Foundation of China (52373189, 52025033, 52173010, 22361132530).

■ REFERENCES

(1) Song, W.; Ye, Q.; Chen, Z.; Ge, J.; Xie, L.; Ge, Z. Advances in Stretchable Organic Photovoltaics: Flexible Transparent Electrodes and Deformable Active Layer Design. *Adv. Mater.* **2024**, *36* (37), No. 2311170.

(2) Guan, S.; Li, Y.; Xu, C.; Yin, N.; Xu, C.; Wang, C.; Wang, M.; Xu, Y.; Chen, Q.; Wang, D.; et al. Self-Assembled Interlayer Enables High-Performance Organic Photovoltaics with Power Conversion Efficiency Exceeding 20%. *Adv. Mater.* **2024**, *36* (25), No. 2400342.

(3) Wang, Z.; Bo, Y.; Bai, P.; Zhang, S.; Li, G.; Wan, X.; Liu, Y.; Ma, R.; Chen, Y. Self-sustaining personal all-day thermoregulatory clothing using only sunlight. *Science* **2023**, *382* (6676), 1291−1296.

(4) Zhu, L.; Zhang, M.; Zhou, G.; Wang, Z.; Zhong, W.; Zhuang, J.; Zhou, Z.; Gao, X.; Kan, L.; Hao, B.; et al. Achieving 20.8% organic solar cells via additive-assisted layer-by-layer fabrication with bulk p-i-n structure and improved optical management. *Joule* **2024**, *8* (11), 3153−3168.

(5) Chen, H.; Huang, Y.; Zhang, R.; Mou, H.; Ding, J.; Zhou, J.; Wang, Z.; Li, H.; Chen, W.; Zhu, J.; et al. Organic solar cells with 20.82% efficiency and high tolerance of active layer thickness through crystallization sequence manipulation. *Nat. Mater.* **2025**, *24* (3), 444−453.

(6) Sun, Y.; Wang, L.; Guo, C.; Xiao, J.; Liu, C.; Chen, C.; Xia, W.; Gan, Z.; Cheng, J.; Zhou, J.; et al. π-Extended Nonfullerene Acceptor for Compressed Molecular Packing in Organic Solar Cells To Achieve over 20% Efficiency. *J. Am. Chem. Soc.* **2024**, *146* (17), 12011−12019.

(7) Zhang, C.; Zhang, M.; Zhou, Q.; Chen, S.; Kim, S.; Yao, J.; Zhang, Z.; Bai, Y.; Chen, Q.; Chang, B.; et al. Diffusion-Limited Accepter Alloy Enables Highly Efficient and Stable Organic Solar Cells. *Adv. Funct. Mater.* **2023**, *33* (18), No. 2214392.

(8) Sun, C.; Lee, J.-W.; Lee, C.; Lee, D.; Cho, S.; Kwon, S.-K.; Kim, B. J.; Kim, Y.-H. Dimerized small-molecule acceptors enable efficient and stable organic solar cells. *Joule* **2023**, *7* (2), 416−430.

(9) Xiao, M.; Wang, C.; Xu, Y.; Zhang, W.; Fu, Z.; Qiao, J.; Wang, H.; Xia, X.; Zhang, M.; Qin, W.; et al. Enhance Photo-Stability of Up-Scalable Organic Solar Cells: Suppressing Radical Generation in Polymer Donors. *Adv. Mater.* **2025**, *37* (5), No. 2412746.

(10) Liang, Y.; Zhang, D.; Wu, Z.; Jia, T.; Lüer, L.; Tang, H.; Hong, L.; Zhang, J.; Zhang, K.; Brabec, C. J.; et al. Organic solar cells using oligomer acceptors for improved stability and efficiency. *Nat. Energy* **2022**, *7* (12), 1180−1190.

(11) Wu, X.; Cai, S.; Shen, K.; Chen, M.; Wang, T.; Zhao, X.; Wang, S.; Yang, X.; Zhang, M.; Sun, R.; Min, J. A double-cable Y-series-based

polymer acceptor for efficient all-polymer solar cells: a new strategy of polymerizing small molecule acceptors. *J. Mater. Chem. C* **2023**, *11* (10), 3533−3541.
(12) Bai, Y.; Zhang, Z.; Zhou, Q.; Geng, H.; Chen, Q.; Kim, S.; Zhang, R.; Zhang, C.; Chang, B.; Li, S.; et al. Geometry design of tethered small-molecule acceptor enables highly stable and efficient polymer solar cells. *Nat. Commun.* **2023**, *14* (1), No. 2926.
(13) Liu, H.; Tang, L.; Li, T.; Yi, F.; Su, W.; Xiang, K.; Dong, B.; Yao, Z.; Wang, K.; Hu, T.; et al. Hybrid Linking Sites Constructed Non-Fully Conjugated Asymmetric Dimerized Giant Molecule Acceptors for Organic Solar Cells with an Efficiency of ≈20%. *Angew. Chem., Int. Ed.* **2025**, *64* (19), No. e202503721.
(14) Li, Y.; Ge, Z.; Mei, L.; Ma, H.; Chen, Y.; Wang, X.; Yu, J.; Lu, G.; Yang, R.; Chen, X.-K.; et al. Isomeric Dimer Acceptors for Stable Organic Solar Cells with over 19% Efficiency. *Angew. Chem., Int. Ed.* **2024**, *63* (50), No. e202411044.
(15) Lv, M.; Wang, Q.; Zhang, J.; Wang, Y.; Zhang, Z.-G.; Wang, T.; Zhang, H.; Lu, K.; Wei, Z.; Deng, D. Strengthening the Hetero-Molecular Interactions in Giant Dimeric Acceptors Enables Efficient Organic Solar Cells. *Adv. Mater.* **2024**, *36* (4), No. 2310046.
(16) Yu, H.; Wang, Y.; Kwok, C. H.; Zhou, R.; Yao, Z.; Mukherjee, S.; Sergeev, A.; Hu, H.; Fu, Y.; Ng, H. M.; et al. A polymer acceptor with double-decker configuration enhances molecular packing for high-performance all-polymer solar cells. *Joule* **2024**, *8* (8), 2304−2324.
(17) Yao, Z.; Wan, X.; Li, C.; Chen, Y. Two-Dimensional Conjugation Extended CH-Series Acceptors with a Distinctive A−D−A Character. *Acc. Mater. Res.* **2023**, *4* (9), 772−785.
(18) Wang, J.; Wang, P.; Chen, T.; Zhao, W.; Wang, J.; Lan, B.; Feng, W.; Liu, H.; Liu, Y.; Wan, X.; et al. Isomerism Effect of 3D Dimeric Acceptors for Non-Halogenated Solvent-Processed Organic Solar Cells with 20% Efficiency. *Angew. Chem., Int. Ed.* **2025**, *64* (12), No. e202423562.
(19) You, S.; Zhang, Y.; Huang, B.; Jeong, S. Y.; Shuai, X.; Huang, S.; Woo, H. Y.; Wu, F.; Chen, L. Linkage Regulation of Back-To-Back Connected Dimers as Guest Acceptors Enables Organic Solar Cells with Excellent Efficiency, Stability and Flexibility. *Adv. Funct. Mater.* **2025**, *35* (6), No. 2414803.
(20) Chen, H.; Kan, B.; Wang, P.; Feng, W.; Li, L.; Zhang, S.; Chen, T.; Yang, Y.; Duan, T.; Yao, Z.; et al. Terminally Chlorinated and Thiophene-linked Acceptor-Donor-Acceptor Structured 3D Acceptors with Versatile Processability for High-efficiency Organic Solar Cells. *Angew. Chem., Int. Ed.* **2023**, *62* (38), No. e202307962.
(21) Li, Y.; Mei, L.; Ge, Z.; Liu, C.; Song, J.; Man, Y.; Gao, J.; Zhang, J.; Tang, Z.; Chen, X.-K.; Sun, Y. Conjugation-Broken Dimer Acceptors Enable High-Efficiency, Stable, and Flexibility-Robust Organic Solar Cells. *Adv. Mater.* **2024**, *36* (35), No. 2403890.
(22) Duan, T.; Feng, W.; Li, Y.; Li, Z.; Zhang, Z.; Liang, H.; Chen, H.; Zhong, C.; Jeong, S.; Yang, C.; et al. Electronic Configuration Tuning of Centrally Extended Non-Fullerene Acceptors Enabling Organic Solar Cells with Efficiency Approaching 19%. *Angew. Chem., Int. Ed.* **2023**, *62* (42), No. e202308832.
(23) Chen, H.; Zou, Y.; Liang, H.; He, T.; Xu, X.; Zhang, Y.; Ma, Z.; Wang, J.; Zhang, M.; Li, Q.; et al. Lowing the energy loss of organic solar cells by molecular packing engineering via multiple molecular conjugation extension. *Sci. China: Chem.* **2022**, *65* (7), 1362−1373.
(24) Zhu, R.; Li, Q.-S.; Li, Z.-S. Nitrogen substitution improves the mobility and stability of electron transport materials for inverted perovskite solar cells. *Nanoscale* **2018**, *10* (37), 17873−17883.
(25) Ding, P.; Chen, Z.; Yang, D.; Yu, X.; Shi, J.; Chen, Y.; Zhu, J.; Wu, J.; Cao, X.; Xie, L.; et al. U-Shaped Dimeric Acceptors for Balancing Efficiency and Stability in Organic Solar Cells. *Adv. Mater.* **2025**, *37* (9), No. 2414080.
(26) Zeng, L.; Hu, R.; Zhang, M.; Lee, S.; Wang, Q.; Meng, S.; Chen, Q.; Liu, J.; Xue, L.; Mi, L.; et al. Halogen-substituted phenazine cores reduce energy losses and optimize carrier dynamics in tethered acceptors for 19.8% efficient and stable polymer solar cells. *Energy Environ. Sci.* **2025**, *18* (13), 6754−6763.
(27) Li, S.; Zhang, R.; Zhang, M.; Yao, J.; Peng, Z.; Chen, Q.; Zhang, C.; Chang, B.; Bai, Y.; Fu, H.; et al. Tethered Small-Molecule Acceptors Simultaneously Enhance the Efficiency and Stability of Polymer Solar Cells. *Adv. Mater.* **2023**, *35* (2), No. 2206563.
(28) Song, W.; Ye, Q.; Yang, S.; Xie, L.; Meng, Y.; Chen, Z.; Gu, Q.; Yang, D.; Shi, J.; Ge, Z. Ultra Robust and Highly Efficient Flexible Organic Solar Cells with Over 18% Efficiency Realized by Incorporating a Linker Dimerized Acceptor. *Angew. Chem., Int. Ed.* **2023**, *62* (41), No. e202310034.
(29) Zhang, M.; Wang, Z.; Zhu, L.; Zeng, R.; Xue, X.; Liu, S.; Yan, J.; Yang, Z.; Zhong, W.; Zhou, G.; et al. Jamming Giant Molecules at Interface in Organic Photovoltaics to Improve Performance and Stability. *Adv. Mater.* **2024**, *36* (52), No. 2407297.
(30) Liang, H.; Ma, K.; Ding, S.; Zhao, W.; Si, X.; Cao, X.; Yao, Z.; Duan, T.; Long, G.; Li, C.; et al. A Pyrazinyl Wide-Bandgap Polymer Donor Yields 19.35% Efficiency in Tandem Organic Solar Cells. *Adv. Energy Mater.* **2024**, *14* (42), No. 2402370.
(31) Ghasemi, M.; Hu, H.; Peng, Z.; Rech, J. J.; Angunawela, I.; Carpenter, J. H.; Stuard, S. J.; Wadsworth, A.; McCulloch, I.; You, W.; Ade, H. Delineation of Thermodynamic and Kinetic Factors that Control Stability in Non-fullerene Organic Solar Cells. *Joule* **2019**, *3* (5), 1328−1348.
(32) Hu, H.; Ghasemi, M.; Peng, Z.; Zhang, J.; Rech, J. J.; You, W.; Yan, H.; Ade, H. The Role of Demixing and Crystallization Kinetics on the Stability of Non-Fullerene Organic Solar Cells. *Adv. Mater.* **2020**, *32* (49), No. 2005348.
(33) Li, Y.; Qi, F.; Fan, B.; Liu, K.-K.; Yu, J.; Fu, Y.; Liu, X.; Wang, Z.; Zhang, S.; Lu, G.; et al. Eliminating the Burn-in Loss of Efficiency in Organic Solar Cells by Applying Dimer Acceptors as Supramolecular Stabilizers. *Adv. Mater.* **2024**, *36* (23), No. 2313393.
(34) Chen, L.; Zhao, C.; Yu, H.; Sergeev, A.; Zhu, L.; Ding, K.; Fu, Y.; Ng, H. M.; Kwok, C. H.; Zou, X.; et al. Tailoring Cyano Substitutions on Quinoxaline-based Small-Molecule Acceptors Enabling Enhanced Molecular Packing for High-Performance Organic Solar Cells. *Adv. Energy Mater.* **2024**, *14* (30), No. 2400285.
(35) Wan, J.; Wang, T.; Sun, R.; Wu, X.; Wang, S.; Zhang, M.; Min, J. Enabling Highly Efficient and Thermal-Stable Polymer Solar Cells through Semi-Alloy Acceptors Composed of a Hinge-Like Dimer: A Versatile Doping Protocol. *Adv. Mater.* **2023**, *35* (36), No. 2302592.
(36) Vollbrecht, J.; Lee, J.; Ko, S.-J.; Brus, V. V.; Karki, A.; Le, W.; Seifrid, M.; Ford, M. J.; Cho, K.; Bazan, G. C.; Nguyen, T. Q. Design of narrow bandgap non-fullerene acceptors for photovoltaic applications and investigation of non-geminate recombination dynamics. *J. Mater. Chem. C* **2020**, *8* (43), 15175−15182.
(37) Cao, X.; Wang, P.; Jia, X.; Zhao, W.; Chen, H.; Xiao, Z.; Li, J.; Bi, X.; Yao, Z.; Guo, Y.; et al. Rebuilding Peripheral F, Cl, Br Footprints on Acceptors Enables Binary Organic Photovoltaic Efficiency Exceeding 19.7%. *Angew. Chem., Int. Ed.* **2025**, *64* (5), No. e202417244.
(38) Vollbrecht, J.; Brus, V. V. On the recombination order of surface recombination under open circuit conditions. *Org. Electron.* **2020**, *86*, No. 105905.
(39) Liu, J.; Chen, S.; Qian, D.; Gautam, B.; Yang, G.; Zhao, J.; Bergqvist, J.; Zhang, F.; Ma, W.; Ade, H.; et al. Fast charge separation in a non-fullerene organic solar cell with a small driving force. *Nat. Energy* **2016**, *1* (7), No. 16089.
(40) Li, C.; Song, J.; Lai, H.; Zhang, H.; Zhou, R.; Xu, J.; Huang, H.; Liu, L.; Gao, J.; Li, Y.; et al. Non-fullerene acceptors with high crystallinity and photoluminescence quantum yield enable > 20% efficiency organic solar cells. *Nat. Mater.* **2025**, *24* (3), 433−443.
(41) Yao, J.; Kirchartz, T.; Vezie, M. S.; Faist, M. A.; Gong, W.; He, Z.; Wu, H.; Troughton, J.; Watson, T.; Bryant, D.; Nelson, J. Quantifying Losses in Open-Circuit Voltage in Solution-Processable Solar Cells. *Phys. Rev. Appl.* **2015**, *4* (1), No. 014020.
(42) Zhu, L.; Zhang, M.; Xu, J.; Li, C.; Yan, J.; Zhou, G.; Zhong, W.; Hao, T.; Song, J.; Xue, X.; et al. Single-junction organic solar cells with over 19% efficiency enabled by a refined double-fibril network morphology. *Nat. Mater.* **2022**, *21* (6), 656−663.

https://doi.org/10.1021/jacs.5c20384
J. Am. Chem. Soc. 2026, 148, 10714−10724

(43) Ding, Y.; Memon, W. A.; Zhang, D.; Zhu, Y.; Xiong, S.; Wang, Z.; Liu, J.; Li, H.; Lai, H.; Shao, M.; He, F. Dimerized Acceptors with Conjugate-Break Linker Enable Highly Efficient and Mechanically Robust Organic Solar Cells. *Angew. Chem., Int. Ed.* **2024**, *63* (22), No. e202403139.
(44) Zhang, Z.; Yuan, S.; Chen, T.; Wang, J.; Yi, Y.-Q.-Q.; Zhao, B.; Li, M.; Yao, Z.; Li, C.; Wan, X.; et al. Rational design of flexible-linked 3D dimeric acceptors for stable organic solar cells demonstrating 19.2% efficiency. *Energy Environ. Sci.* **2024**, *17* (15), 5719−5729.

https://doi.org/10.1021/jacs.5c20384
J. Am. Chem. Soc. 2026, 148, 10714−10724